




Article

# Co<sub>2</sub>TiO<sub>4</sub>/Reduced Graphene Oxide Nanohybrids for Electrochemical Sensing Applications

Constanza J. Venegas<sup>1,2</sup>, Fabiana A. Gutierrez<sup>3</sup>, Marcos Eguílaz<sup>3</sup>, José F. Marco<sup>4</sup>,  
Nik Reeves-McLaren<sup>5</sup>, Gustavo A. Rivas<sup>3,\*</sup>, Domingo Ruiz-León<sup>2,\*</sup> and Soledad Bollo<sup>1,6,\*</sup> 

<sup>1</sup> Redox Processes Research Centre (CiPRex), Facultad de Ciencias Químicas y Farmacéuticas, Universidad de Chile, Sergio Livingstone 1007, Independencia, Santiago 8380492, Chile; constanza.jvenegas@gmail.com

<sup>2</sup> Laboratorio de Físicoquímica y Electroquímica del estado Sólido, Facultad de Química y Biología, Universidad de Santiago de Chile, Av. Libertador Bernardo O'Higgins n° 3363, Santiago 9160000, Chile

<sup>3</sup> INFIQC, Departamento de Físicoquímica, Facultad de Ciencias Químicas, Universidad Nacional de Córdoba, Ciudad Universitaria, Córdoba 5000, Argentina; fabigutierrez@gmail.com (F.A.G.); marcos.eguilaz@hotmail.com (M.E.)

<sup>4</sup> Instituto de Química Física Rocasolano, CSIC, Calle Serrano 119, 28006 Madrid, Spain; jfmarco@iqfr.csic.es

<sup>5</sup> Department of Materials Science and Engineering, University of Sheffield, Sheffield S1 3JD, UK; n.reeves@sheffield.ac.uk

<sup>6</sup> Advanced Center for Chronic Diseases (ACCDiS), Facultad de Ciencias Químicas y Farmacéuticas, Universidad de Chile, Santiago 8380494, Chile

\* Correspondence: grivas@fcq.unc.edu.ar (G.A.R.); domingo.ruiz@usach.cl (D.R.-L.); sbollo@ciq.uchile.cl (S.B.)

Received: 30 September 2019; Accepted: 8 November 2019; Published: 13 November 2019



**Abstract:** For the first time, the synthesis, characterization, and analytical application for hydrogen peroxide quantification of the hybrid materials of Co<sub>2</sub>TiO<sub>4</sub> (CTO) and reduced graphene oxide (RGO) is reported, using in situ (CTO/RGO) and ex situ (CTO+RGO) preparations. This synthesis for obtaining nanostructured CTO is based on a one-step hydrothermal synthesis, with new precursors and low temperatures. The morphology, structure, and composition of the synthesized materials were examined using scanning electron microscopy, X-ray diffraction (XRD), neutron powder diffraction (NPD), and X-ray photoelectron spectroscopy (XPS). Rietveld refinements using neutron diffraction data were conducted to determine the cation distributions in CTO. Hybrid materials were also characterized by Brunauer–Emmett–Teller adsorption isotherms, Scanning Electron microscopy, and scanning electrochemical microscopy. From an analytical point of view, we evaluated the electrochemical reduction of hydrogen peroxide on glassy carbon electrodes modified with hybrid materials. The analytical detection of hydrogen peroxide using CTO/RGO showed 11 and 5 times greater sensitivity in the detection of hydrogen peroxide compared with that of pristine CTO and RGO, respectively, and a two-fold increase compared with that of the RGO+CTO modified electrode. These results demonstrate that there is a synergistic effect between CTO and RGO that is more significant when the hybrid is synthesized through in situ methodology.

**Keywords:** Hybrid materials; Co<sub>2</sub>TiO<sub>4</sub>; reduced graphene oxide; ex situ synthesis; in situ synthesis; H<sub>2</sub>O<sub>2</sub> detection; electrochemical sensors

## 1. Introduction

In the last decade, nanomaterial technology has grown, in particular driven by the special properties of nanomaterials [1–23]. Currently, the mixture of different types of nanomaterials among metals, metal oxides, nanoclays, quantum carbon nanodots, and carbonaceous materials such as graphene, reduced graphene oxide, and nanosilica, has allowed the generation of new hybrid structures, widening their spectrum of applications [3,4]. Thus, the fabrication of hybrid materials via electrocatalysis has

improved, especially for the design of new electrochemical sensors and for performing analytical tests [5–7]. In particular, some of these advantages, including enhanced surface kinetics and accelerated electrochemical reactions, can be achieved by using new nanomaterials in electrode modifications; furthermore, the addition of carbonaceous nanomaterials enhances the adsorption of the analyte on the electrode surface, helping achieve even quantification [8].

As a component of hybrid architectures, reduced graphene oxide (RGO) is an important carbon-based nanomaterial (CBNM) used for the development of optimized sensors. RGO presents very interesting properties, such as excellent electrical conductivity, high specific surface area, and good mechanical strength, making it possible to obtain a fast and sensitive electrochemical response [9–13]. RGO has been used as a support for nanoparticles, improving the electrocatalytic performance of RGO and avoiding nanoparticle agglomeration [14,15]. The CBNM–inorganic oxide hybrid materials induce an additional electrochemical catalytic ability and may provide further functionalization ability. Many examples of these hybrid materials can be found in the literature, where CBNMs are combined with metal nanomaterials (mainly Au, Ag, Pd, and Pt) [16,17], oxides such as  $\text{Fe}_3\text{O}_4$ ,  $\text{MnO}_2$ ,  $\text{Ni}(\text{OH})_2$ ,  $\text{ZnO}$ ,  $\text{SnO}_2$ ,  $\text{Co}(\text{OH})_2$ , and  $\text{TiO}_2$  [18–23], and chalcogenides such as  $\text{CdS}$ ,  $\text{CdSe}$ , and  $\text{MoS}_2$  [24]. The use of these materials has attracted research efforts due to their considerable potential as enhanced materials for sensing applications. Sensors based on carbon–inorganic oxide composites need (i) the inorganic phase to remain stable in ambient conditions without any structural change, (ii) metal species with more than one oxidation state, and (iii) need to be good conductors of charge carriers (ions and electrons) [25].

In CBNM–inorganic oxide hybrids for sensors, distribution of the inorganic phase and carbon-based material on the surface is important for optimal chemical performance of the as-prepared electrode, so their synthesis must consider several factors. The synthesis methods for these new composite materials are generally classified as *ex situ* and *in situ* [26]. The *ex situ* method involves a mixture of CBNM and previously synthesized nanocrystals, either from the inorganic phase or commercially available in solutions. Although in *ex situ* methods it is possible to preselect nanostructures with desired functionalities, the generated hybrid material sometimes suffers from non-uniform coverage or low density of the nanostructures on the electrode surface. In contrast, *in situ* methods generally give better coverage of nanocrystals on surfaces by controlling the nucleation sites on CBNM via surface functionalization. Thus, a continuous film of nanoparticles (NPs) on CBNM surfaces can be obtained. The literature reports show an array of different strategies for preparing oxide nanocomposites, such as sol-gel and solid-state techniques, chemical bath deposition, hydrothermal synthesis, and chemical vapour deposition [23,27–31]. Among these, most methods for the production of nanosized oxides are based on either co-precipitation or hydrothermal methods.

Spinel ferrites have received significant attention in electrochemical sensor applications [21,32,33]. They present interesting physical electronic, optical, and magnetic properties that make them very interesting nanomaterials. Other kinds of oxides that contain cobalt in the structure have also attracted attention, with  $\text{Co}_3\text{O}_4$  being widely studied either alone or as a composite with graphene [34,35]. An interesting study published by Qi et al. [34] highlighted the formation of  $\text{Co}_3\text{O}_4$  nanorod/graphene composites for the detection of a specific DNA sequence.

In recent years, there has been increasing interest in the use of hybrid materials combining inorganic oxides and graphene, specifically for the electrochemical detection of hydrogen peroxide, with studies focusing on  $\text{Co}_2\text{SnO}_4/\text{RGO}$  [36],  $\text{Pt-CeO}_2/\text{graphene oxide}$  [37],  $\text{Ni}_x\text{Co}_{3-x}\text{N}/\text{nitrogen-doped graphene}$  [38], and  $\text{RGO-SnO}_2$  [39]. The rapid and accurate determination of hydrogen peroxide has an important role in the electron transfer process of hundreds of enzymes in biological systems [40] connected with the oxidation of by-products of glutamate, oxalate, cholesterol, D-amino acid, urate, lactate, lysine, and glucose, as well as in various types of industries, such as paper, textile, pharmaceutical, and environmental industries [41].

Considerable research has focused on compounds with spinel-type structures [27–30,42,43]. Ferrite spinels have been the most studied and have been reported in a large number of publications due

to their versatile applications, including catalytic functions [43,44]. However, there are no reports on the synthesis of  $\text{Co}_2\text{TiO}_4/\text{RGO}$  nanocomposites or their application as electrode materials for electrochemical sensors.

According to the literature,  $\text{Co}_2\text{TiO}_4$  (CTO) can be synthesized using various methods (e.g., co-precipitation [45,46], solid-state [47–49] or solvothermal syntheses [50]) that always involve a final high-temperature calcination step. In this report, we discuss the fabrication of CTO at reduced temperatures using a hydrothermal synthesis and new precursors, which allow the formation of single-phase CTO in one step. Only a few applications have been reported for CTO, such as the degradation of water pollutants [50] and as anodes in batteries [51]; however, no applications have been reported in the field of electrochemical sensors.

In this work, we propose two methods for the formation of CTO and RGO hybrids, namely *in situ* (CTO/RGO) and *ex situ* (CTO+RGO) methods, to be used for the development of hydrogen peroxide sensors. We determine the catalytic effect of these materials for hydrogen peroxide reduction and their application in the electrochemical detection of hydrogen peroxide ( $\text{H}_2\text{O}_2$ ) in real samples.

## 2. Experimental Section

### 2.1. Chemical Reagents

Cobalt chloride hexahydrate (Sigma Aldrich, San Luis, MO, USA, 98%), titanium tetrachloride (Sigma Aldrich, San Luis, MO, USA, 99.9%), sodium hydroxide (Merck, Darmstadt Germany, 98%), and hydrogen peroxide (Merck, Darmstadt Germany, Germany, 30%) were used as received. Reduced Graphene oxide (RGO) was obtained from Graphenea<sup>®</sup> (San Sebastian, Spain). Details of the elemental analysis and X-ray fluorescence spectrometric analysis of RGO are included in Supplementary Materials (Tables S1 and S2). Nafion<sup>®</sup> was purchased from Sigma Aldrich (San Luis, Mo, USA). A pH 12 NaOH solution was used as the supporting electrolyte. All solutions were prepared with ultrapure water ( $\rho = 18 \text{ M}\Omega \text{ cm}$ ) from a Millipore Milli-Q system.

### 2.2. Synthesis of the Nanohybrids

**Synthesis of CTO:** CTO nanoparticles were obtained by a hydrothermal method. Cobalt chloride ( $\text{CoCl}_2 \cdot 6\text{H}_2\text{O}$ ) and titanium tetrachloride ( $\text{TiCl}_4$ ) were dissolved in deionized water to form two transparent solutions. The  $\text{TiCl}_4$  solution was slowly added to an ice cold cobalt chloride solution in a 2:1 target molar ratio of Co/Ti. The NaOH solution was added dropwise to the mixture under magnetic stirring until a concentration of 2.0 M was reached. The reaction was stirred at room temperature for 30 min, and the resulting slurry was then transferred into a 23 mL Teflon-lined stainless steel autoclave. The mixture was exposed to hydrothermal conditions at 250 °C for up to 12 h. The resulting product was collected by centrifugation, washed with deionized water and absolute ethanol several times, and then dried at 80 °C.

**Ex situ synthesis of CTO+RGO:** RGO was mechanically mixed with the CTO nanoparticles in an agate mortar at a ratio of 80:20.

**In situ synthesis of CTO/RGO:** The same procedure was used for the synthesis of the CTO, but after mixing all the precursors, RGO was added. The hydrothermal syntheses then proceeded using the same time and temperature conditions.

### 2.3. Modification of Glassy Carbon Electrodes (GCEs) with the Nanohybrid Materials

To modify the GCEs, a portion of the hybrid material (CTO+RGO or CTO/RGO) was dispersed in 1.00 mL of Nafion<sup>®</sup> (0.2% *v/v* in ethanol) by sonication for 30 min. Prior to surface modification, the GCEs were polished with 0.3 and 0.05  $\mu\text{m}$  alumina slurries for 1 min. Immobilization of the hybrid nanomaterials was achieved by drop casting 10  $\mu\text{L}$  of the dispersion onto the GCE, followed by evaporating the solvent at room temperature.

#### 2.4. Characterization

Room temperature time-of-flight (ToF) neutron powder diffraction (ND) data were collected on the General Material diffractometer (GEM) in a vanadium canister at the ISIS ((Neutron and Muon Source) facility, Rutherford Appleton Laboratory (RAL), Oxford. Data were collected in the backscattering detector bank (50.07°–74.71°). X-ray diffraction (XRD) data were collected in a PANalytical X'Pert<sup>3</sup> Powder diffractometer with Cu K $\alpha$  radiation. Rietveld refinement was performed using the (graphical user interface for GSAS experiment, XPGUI [52] for GSAS (Generalized Structure Analysis System) [53] and both XRD and ND data. Raman measurements were recorded with a WiTec Alpha 300 Raman-AFM using a 532 nm laser.

X-ray photoelectron spectroscopy (XPS) data were recorded with a PHOIBOS 150 hemispherical analyzer (SPECS) under a pressure lower than  $2 \times 10^{-9}$  mbar using Al K $\alpha$  radiation and constant pass energy values of 100 eV and 20 eV for the wide and narrow scans, respectively. The binding energy (BE) scale was referenced to the main C 1s signal (284.6 eV) corresponding to the contamination layer. Atomic ratios were calculated using MultiQuant XPS software [54], with the different spectral areas obtained by peak integration after background subtraction using the Shirley method.

The surface morphology was obtained by scanning electron microscopy (SEM) (TESCAN, Czech Republic, Vega 3 model). Histogram size distribution was calculated using ImageJ software. A compositional study was conducted by analysis of energy dispersive spectroscopy (EDS) using a Bruker probe (model QUANTAX 400a series).

Thermogravimetric analysis was carried out with a Shimadzu DTG-60 instrument in a flowing air atmosphere with an increase of  $10\text{ }^{\circ}\text{C min}^{-1}$  in platinum canisters. The reference used was  $\alpha$ -alumina.

Scanning electrochemical microscopy (SECM) images were obtained with a CHI900 bipotentiostat (CHI Instruments, Dallas, TX, USA) using a  $10\text{ }\mu\text{m}$  diameter platinum ultra-micro-electrode (UME) probe. The SECM feedback mode was selected to obtain images of each modified surface using a  $5.00 \times 10^{-4}$  M ferrocene methanol (FcOH) solution. The UME and the substrate potentials were held at 0.50 V and 0.10 V, respectively, during the acquisition of the images, the UME scan rate was  $10.0\text{ }\mu\text{m s}^{-1}$ . The SECM surface plots were depicted by normalizing the current of the UME at the surface ( $i$ ) with the steady-state current of the UME positioned far from the substrate ( $i_0$ ).

Textural properties were obtained from the adsorption–desorption isotherm of N<sub>2</sub> at 77 K, which was carried out using a Micromeritics 3Flex. The sample was previously degassed for 10 h at 76.9 K under vacuum using a Micromeritic SmartVacPrep. The specific surface area was determined from the adsorption branch in the range of  $0.05 \leq p/p_0 \leq 0.25$  using the Brunauer–Emmett–Teller (BET) theory [55].

Electrochemical impedance spectroscopy (EIS), cyclic voltammetry, amperometry, and polarization curves were performed with a three-electrode cell. Ag/AgCl, 3.0 M KCl (CH Instrument), and platinum wire were used as the reference electrode, electrolyte, and auxiliary electrode, respectively. The working electrode was a glassy carbon electrode (GCE, CH. Instrument) modified with our hybrid materials. Electrochemical impedance spectroscopy (EIS) measurements were performed with an Autolab PGSTAT 128 N potentiostat (EcoChemie) in a frequency range of 10.000 Hz –0.1 Hz (amplitude:  $\sim 10$  mV). The redox probe was 0.010 M hydrogen peroxide prepared in pH 12 NaOH, and the working potential was  $-0.400$  V. The impedance spectra were analysed using Z-view software.

Amperometric and voltammetric experiments were performed using a Palm Sens potentiostat (The Netherlands). The amperometric experiments were conducted in deoxygenated pH 12 NaOH solution at  $-0.400$  V by applying the desired working potential and allowing the transient currents to decay to a steady-state value prior to the addition of 0.10 mM H<sub>2</sub>O<sub>2</sub>, with subsequent current monitoring.

Polarization curves were performed in a Bioanalytical Systems, Inc, BAS®(West Lafayette, IN, USA) Model CV 50 W potentiostat at 0.005 V/s using 1.0 mM hydrogen peroxide solution in deoxygenated pH 12 NaOH solution. The rotating disk speed was maintained at 1600 rpm.

### 3. Results and Discussion

#### 3.1. Physicochemical Characterization

Phase analysis was performed using XRD. Figure 1 shows the diffraction patterns for pristine CTO and both CTO/RGO and CTO+RGO specimens. In all cases, the observed Bragg reflections were indexed against the International Centre for Diffraction Data (ICDD) database entry for  $\text{Co}_2\text{TiO}_4$  (ICDD PDF # 00-018-0428). There were no additional peaks observed that might have been attributable to contaminants or unreacted precursors. The characteristic Bragg peak for RGO (002, a  $2\theta = 24^\circ$ ) was not observed, suggesting that RGO sheets were not homogeneously dispersed and coated with CTO [56,57], or that its percentage in the hybrids was very low [58,59]. On the other hand, these results confirm that CTO can be obtained using the hydrothermal method with the new precursors,  $\text{TiCl}_4$  and  $\text{CoCl}_2 \cdot 6\text{H}_2\text{O}$ , in a single step. There was no need for high-temperature calcination. The pure CTO was subsequently mixed with RGO to obtain the ex situ hybrid.

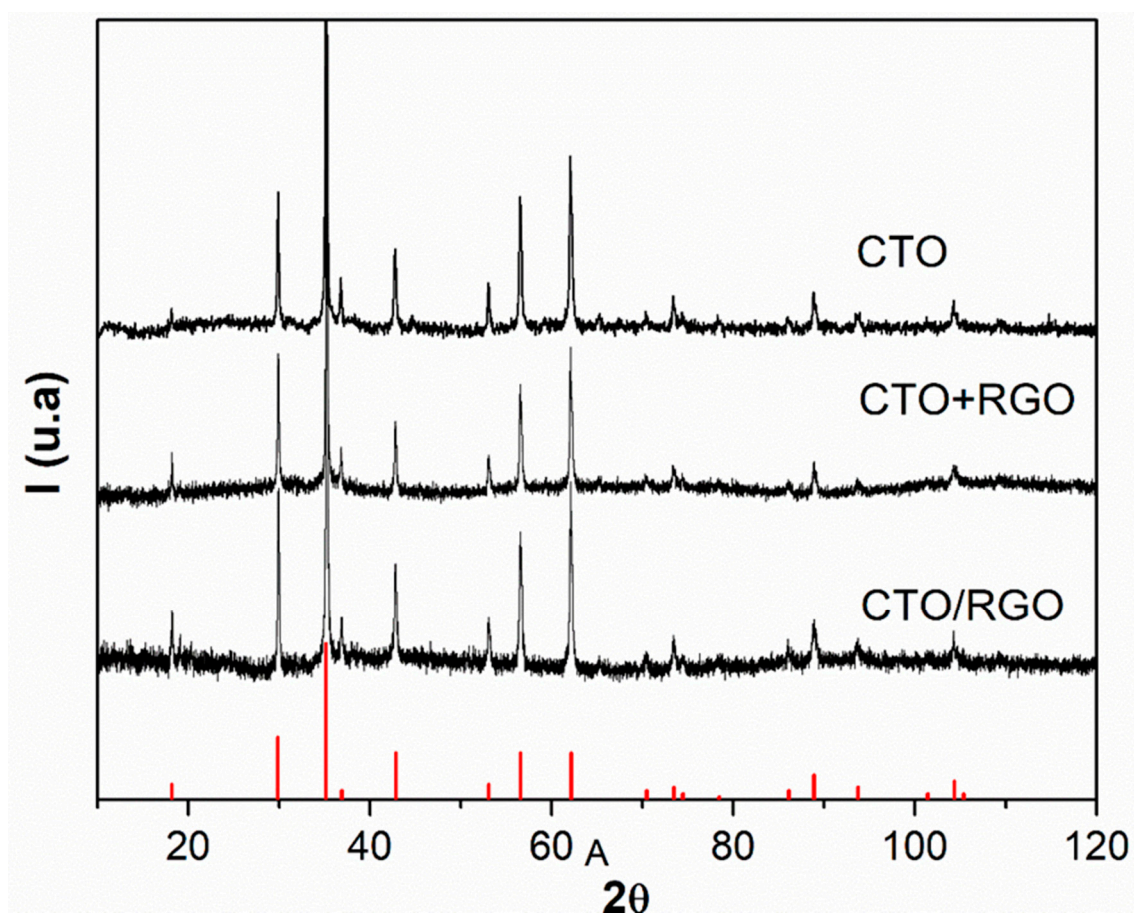


**Figure 1.** Phase analysis of the diffraction patterns for pristine  $\text{Co}_2\text{TiO}_4$  (CTO), CTO/reduced graphene oxide (RGO) (in situ), and CTO+RGO (ex situ). The red diffraction pattern corresponds to CTO (ICDD PDF # 00-018-0428).

To verify the cation distribution within the CTO spinel structure contained in the hybrids, we performed a structural refinement with the Rietveld method using neutron diffraction data. Figure 2 displays the neutron diffraction profiles, which show an inverse spinel-type structure generally described as  $\text{Co}^{\text{Td}}(\text{Co}_{0.5}\text{Ti}_{0.5})_2^{\text{Oh}}\text{O}_4$ , where cobalt and titanium are expected to be present as  $\text{Co}^{2+}$  and  $\text{Ti}^{4+}$ . The CTO was refined in the cubic space group,  $\text{Fd}\bar{3}\text{m}$ .

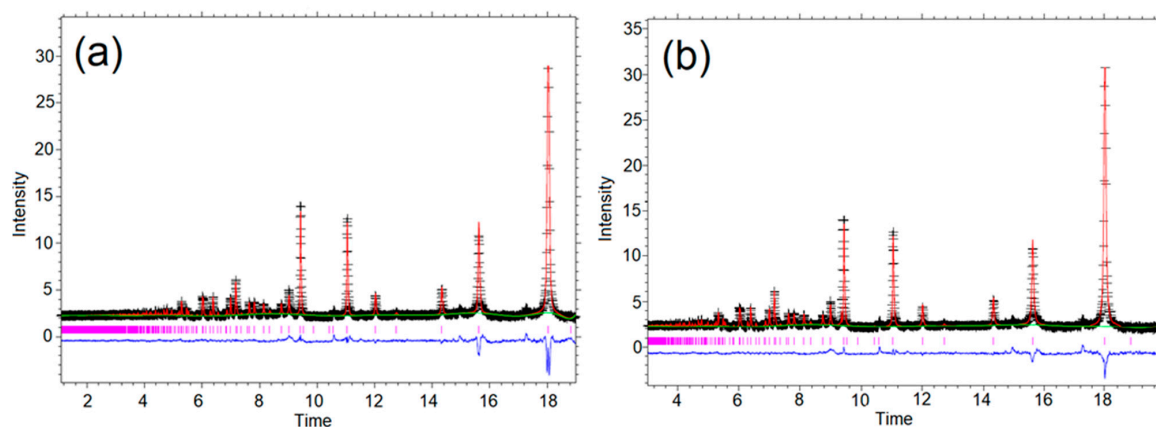


**Figure 2.** Neutron powder diffraction profile of  $\text{Co}_2\text{TiO}_4/\text{RGO}$  from Rietveld refinements using GSAS+EXPGUI at room temperature: CTO/RGO (a) and CTO+RGO (b). The calculated patterns (red) are compared vs. observed data (black +), with the profile difference (observed–calculated) in blue.

The refined parameters are summarized in Table S3. As a starting model, we considered that the  $\text{Co}^{2+}$  ions to be distributed in both crystallographic, tetrahedral, and octahedral sites, with  $\text{Ti}^{4+}$  ions distributed only in octahedral sites. The background was refined first, using a shifted Chebyshev function with 16 terms, followed by the lattice parameters, phase fraction scale factors, and the profile parameters, to model peak broadening largely due to crystallite size effects. Finally, the atomic position in order of the scattering factor for metal sites and  $U_{\text{iso}}$  for oxygen were refined. The process was repeated to convergence, until there were negligible shifts in refined variables. From the occupations observed, it was concluded that the cationic distribution for the CTO in CTO/RGO is  $(\text{Co}_{0.98}\text{Ti}_{0.02})_{\text{Td}}(\text{Co}_{0.96}\text{Ti}_{1.04})_{\text{Oh}}\text{O}_4$  and in CTO+RGO is  $(\text{Co}_{0.96}\text{Ti}_{0.04})_{\text{Td}}(\text{Co}_{0.98}\text{Ti}_{1.02})_{\text{Oh}}\text{O}_4$ . These results indicate that the tetrahedral sites are not fully occupied by  $\text{Co}^{2+}$  ions since there is a small amount of  $\text{Ti}^{4+}$ , unlike the work reported by S. Thota et al., where CTO was synthesized by a solid-state reaction, with  $\text{Co}^{2+}$  and  $\text{Co}^{3+}$  in both crystallographic sites and  $\text{Ti}^{3+}$  in the octahedral site [48,60]. These differences in the distribution of the cations in the crystallographic sites can be attributed to the method of synthesis and the precursors used, suggesting that the lower reaction temperature possibly means there is insufficient energy to permit full ordering or mixing of the cations, and thus some inhomogeneity persists.

On the other hand, for CTO/RGO and CTO+RGO, similar cell parameter values were calculated from the Rietveld refinements, with  $a = 8.4519(1) \text{ \AA}$  and  $a = 8.4554(1) \text{ \AA}$ , respectively. The refined values of the lattice parameters were somewhat larger than previously reported for CTO ( $a = 8.440 \text{ \AA}$ , ICDD PDF # 00-018-0428), probably due to the formation of a  $\text{Co}_{2-x}\text{Ti}_{1+x}\text{O}_4$  solid solution with a small Ti excess [51].

The presence of RGO in the hybrid CTO/RGO was determined by Raman spectroscopy. Figure S1 shows the D band at  $1345 \text{ cm}^{-1}$  and the G band at  $1593 \text{ cm}^{-1}$ , which is characteristic of carbonaceous materials [61]. The integrated intensity ratio ( $I_{\text{D}}/I_{\text{G}}$ ) of the D and G bands of CTO/RGO, widely used to characterize the degree of defects in graphitic materials [62], was 2.07. In relation to this, the  $I_{\text{D}}/I_{\text{G}}$  determined for the RGO present in the hybrids was consistent with those previously reported [61], demonstrating a high degree of defects in the graphitic structure.

The chemical compositions of the materials and the valence states of the cations were studied by XPS. The wide scan spectra (not shown) recorded for CTO and CTO/RGO showed only signals corresponding to C, O, Ti, and Co, without contributions from other elements, indicating that the compounds were free from contaminants. The high-resolution Co 2p, Ti 2p, and O 1s spectra recorded for both materials were virtually identical, both in terms of the binding energies of the main spectral features and the shape of the various spectral lines, as observed in Figure 3a–c, respectively.

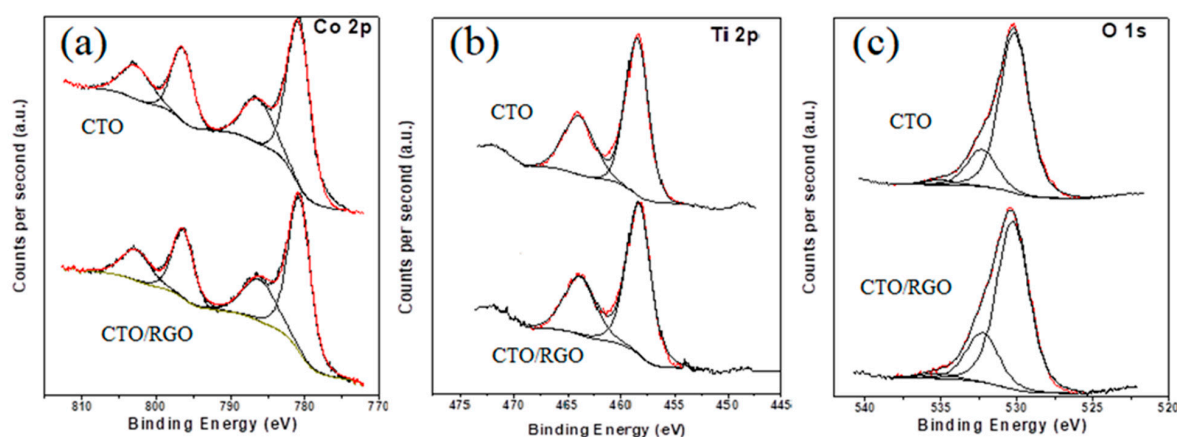


**Figure 3.** Co 2p (a), Ti 2p (b), and O 1s spectra (c) X-ray photoelectron spectroscopy (XPS) spectra for CTO and CTO/RGO materials.

The Co 2p spectra were composed of a relatively narrow spin–orbit doublet (Binding Energy (BE) Co 2p<sub>3/2</sub> = 780.7 eV; BE Co 2p<sub>1/2</sub> = 796.4 eV), accompanied by a strong, “shake-up” satellite structure above the main photoemission lines (786.1 eV and 802.8 eV) (Figure 3a). These binding energy values and the occurrence of the intense satellite features were fully compatible with the presence of Co<sup>2+</sup> [63]. Although the fairly intense satellites suggested that the materials exclusively contained Co<sup>2+</sup>, we explored the possible existence of a Co<sup>3+</sup> contribution, which had been recently observed elsewhere [64]. It is known that oxides with spinel-related structures contain Co<sup>3+</sup> that can be characterized by a spin–orbit doublet with a binding energy of the main Co 2p<sub>3/2</sub> core level of 779.6 eV [63]. Including such a contribution in the spectra presented in Figure 3a proved difficult, with the fit always either giving a negligible intensity for the Co<sup>3+</sup> doublet or unrealistically narrow line widths. Therefore, we can confidently conclude that the oxides prepared in this work contain only Co<sup>2+</sup>.

The Ti 2p spectra recorded for both materials (Figure 3b) showed only a spin–orbit doublet with BE Ti 2p<sub>3/2</sub> = 458.4 eV and BE Ti 2p<sub>1/2</sub> = 463.8 eV. These binding energy values are characteristic of Ti<sup>4+</sup> [65–67]. In principle, as we have demonstrated in previous papers [66–68], Ti<sup>4+</sup> can be easily distinguished from Ti<sup>3+</sup> in a Ti 2p spectrum, and their relative contributions can be determined without problems. In the case of the concomitant presence of Ti<sup>4+</sup> and Ti<sup>3+</sup>, the Ti 2p lines become broad and asymmetric, since Ti<sup>3+</sup> is usually characterized by a spin–orbit doublet appearing at binding energies approximately 1 eV lower than those characteristic of a Ti<sup>4+</sup> spin–orbit doublet. The symmetric character of the Ti 2p spectral lines recorded from the materials prepared in this work ruled out the presence of a Ti<sup>3+</sup> contribution. In conclusion, our low temperature method produced a CTO with only Ti<sup>4+</sup>, in contrast with results recently reported for CTO prepared by a high-temperature solid-state reaction, where Ti presented a trivalent character in this compound [64].

The O 1s spectra (Figure 3c) contain three contributions. The main one (approximately 75%) at 530.1 eV is characteristic of metal–oxygen bonds and has to be associated with the Co–O and Ti–O bonds existing in Co<sub>2</sub>TiO<sub>4</sub> [63,65]. The contribution at 532.3 eV can be assigned to C=O bonds or an array of physi- and chemisorbed water molecules on the surface of the CTO particles. The small contribution (less than 5%) at approximately 535.0 eV is likely due to some unspecific organic moiety.

As reported previously, the difference between the O 1s and Ti 2p<sub>3/2</sub> binding energies is also representative of the oxidation state of titanium [69]. An energy difference between 71.2 and 72.2 eV is characteristic of Ti<sup>4+</sup>, while an energy difference between 72.9 and 73.4 eV is characteristic of Ti<sup>3+</sup>. In the case of the materials considered in this work, the energy differences observed were 71.6 eV (CTO) and 71.9 eV (CTO/RGO) (i.e., both were characteristic of Ti<sup>4+</sup>). It has also been reported that a correlation exists between this energy difference and the Ti–O bond length. In the case of the materials examined here, the energy difference was slightly larger for the composite material, which would imply

the occurrence of slightly longer Ti-O bonds that probably arose from a more distorted coordination geometry [25].

The Co/O and Ti/O atomic ratios obtained from the evaluation of the XPS data were 0.38 and 0.18 for CTO, respectively, and 0.41 and 0.15 for CTO/RGO, respectively. These Co/O and Ti/O atomic ratios, which were calculated while considering that only 75% of the oxygen corresponded to reticular oxygen, were relatively close to the nominal values of 0.5 and 0.25, respectively.

To verify the amount of carbon material present in the CTO/RGO in situ hybrid, a thermogravimetric analysis (TGA) was carried out in a temperature range between 30 and 1000 °C and in an air atmosphere (Figure S2). The steep loss observed at approximately 450 °C (20.8 wt.%) is attributed to the decomposition of the RGO present in the hybrid [57].

Particle morphologies in the hybrid materials were studied by SEM. In both hybrid materials, CTO presented a polyhedral morphology, as shown in Figure 4a,b. However, according to the histogram size distribution shown in Figure S3, both materials have average particle sizes of  $103 \pm 26$  nm and  $103 \pm 43$  nm for CTO/RGO and CTO+RGO, respectively. The in situ synthesis appears to produce a slightly more homogeneous size distribution of CTO nanoparticles in the hybrid material.

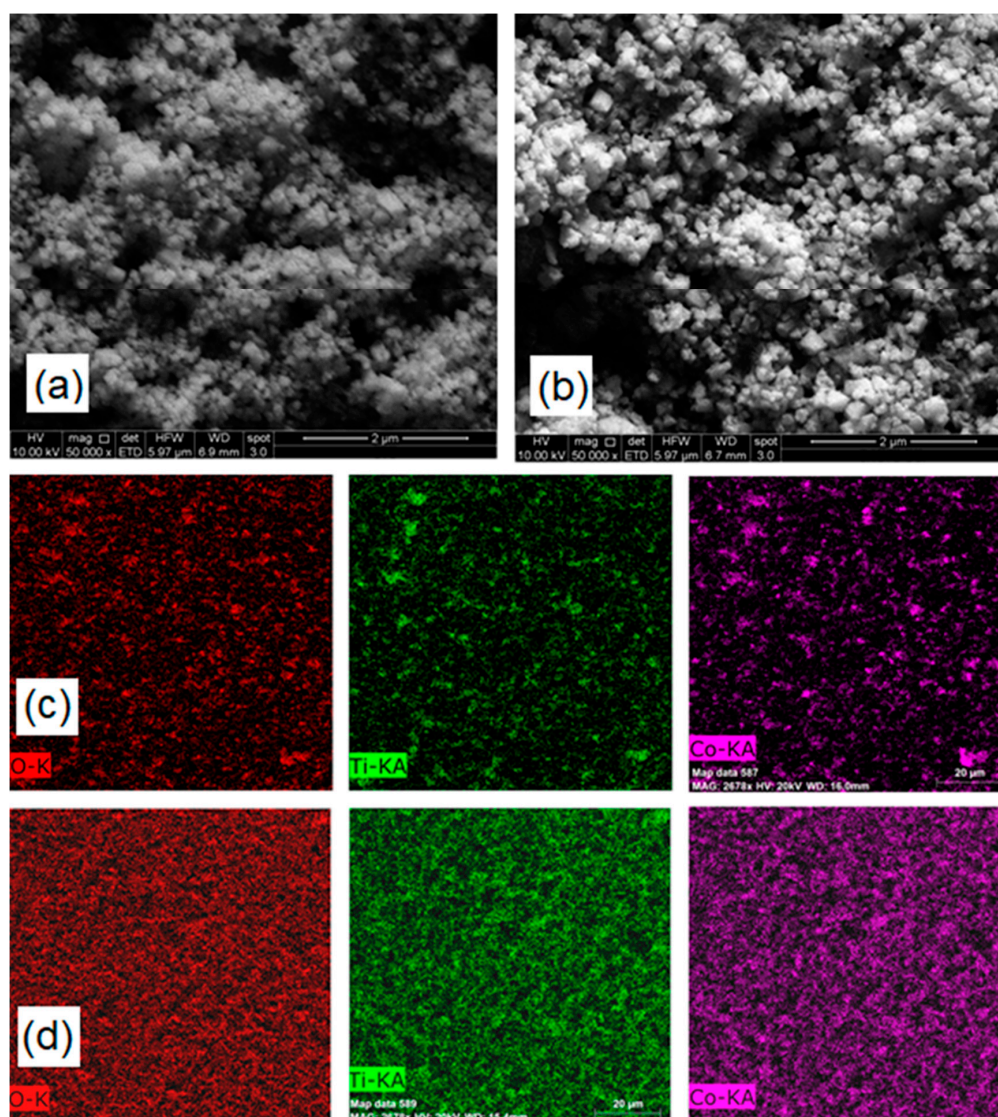


**Figure 4.** SEM micrographs of CTO+RGO (a) and CTO/RGO (b). EDX mapping (oxygen, titanium, and cobalt) of CTO+RGO (c) and CTO/RGO (d).



EDX maps, as shown in Figure 4, were used to study the distribution of Co, Ti, and O in the hybrid materials. Comparison of Figure 4c,d shows that CTO/RGO presents a more homogeneous elemental distribution than CTO+RGO. Since the CTO/RGO method involves the formation and growth of the inorganic material in the presence of the carbonaceous material at the nanometric scale, it enables more uniform distribution of elements in the polycrystalline material by controlling the nucleation sites in the nanomaterials through the functionalization of the surfaces [25].

According to the literature, the oxide nanoparticle synthesis method can affect the particle size and shape, the particle size distribution, and the degree of crystallinity [70]. In our case, the in situ hydrothermal synthesis method produced CTO particles with a narrower size distribution.

The nitrogen sorption isotherms of CTO and both hybrid materials are shown in Figure 5. All the compounds exhibit a typical type IV behaviour with a H2(a) hysteresis loop characteristic of materials that contain mesopores [71]. The presence of RGO in the hybrids produces a large increase in the porosity compared to the CTO.

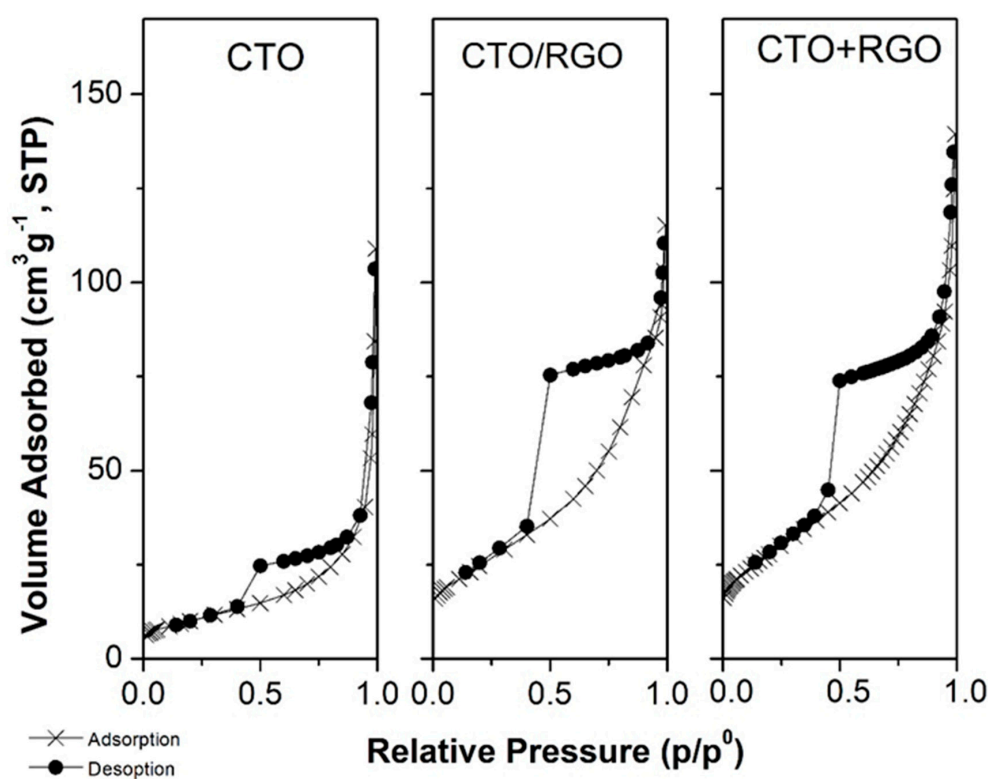


Figure 5. N<sub>2</sub> adsorption–desorption isotherm profile.

The BET specific surface area for pristine CTO synthesized by the hydrothermal method was 36 m<sup>2</sup>/g, higher than the value of 4 m<sup>2</sup>/g reported for CTO synthesized by methods with high calcination temperatures [72]. It is expected that this higher surface area obtained for hydrothermally synthesized CTO will increase the electrocatalytic performance against hydrogen peroxide determination. Table 1 shows the texture analysis corresponding to the hybrid materials. The incorporation of RGO, either in CTO+RGO or CTO/RGO, produces an increase in the BET areas ( $S_{\text{BET}}$ ) to 100 m<sup>2</sup>/g and 90 m<sup>2</sup>/g, respectively. Both hybrids have a similar mesoporous volume ( $V_{\text{m}}$ ); however, the in situ hybrid presents 100% mesoporous-type pores, without any micropore ( $V_0$ ) formation observed; the ex situ hybrid exhibits 86.3% mesopore volume ( $V_{\text{m}}$ ) and 13.7% micropore volume ( $V_0$ ).

**Table 1.** Textural analysis for CTO/RGO and CTO+RGO.

Hybrid Material	$V_0$ (cm <sup>3</sup> /g)	$V_m$	$S_{BET}$ (m <sup>2</sup> /g)
CTO+RGO	0.029	0.182	100
CTO/RGO	0.000	0.173	90

To characterize both the topography and electroactivity of electrodes modified with the hybrid material, scanning electrochemical microscopy (SECM) in feedback mode was used. SECM allowed us to characterize both the topography and electroactivity of newly modified surfaces. Figure 6 displays the normalized currents ( $i/i_0$ ) of UME when scanning the CTO/RGO and CTO+RGO surfaces using FcOH as a redox mediator. The electrode modified with CTO/RGO showed higher normalized currents than the one modified using CTO+RGO. This current increase could be attributed to a better coupling between the components of the hybrid product of in situ synthesis and a better distribution of CTO on the graphitic material, resulting in improved electroactivity. As in previous reports [73,74], there were regions with different electroactivity, probably due to a non-homogeneous dispersion of hybrids that generate areas with dissimilar concentrations on the electrode surface.

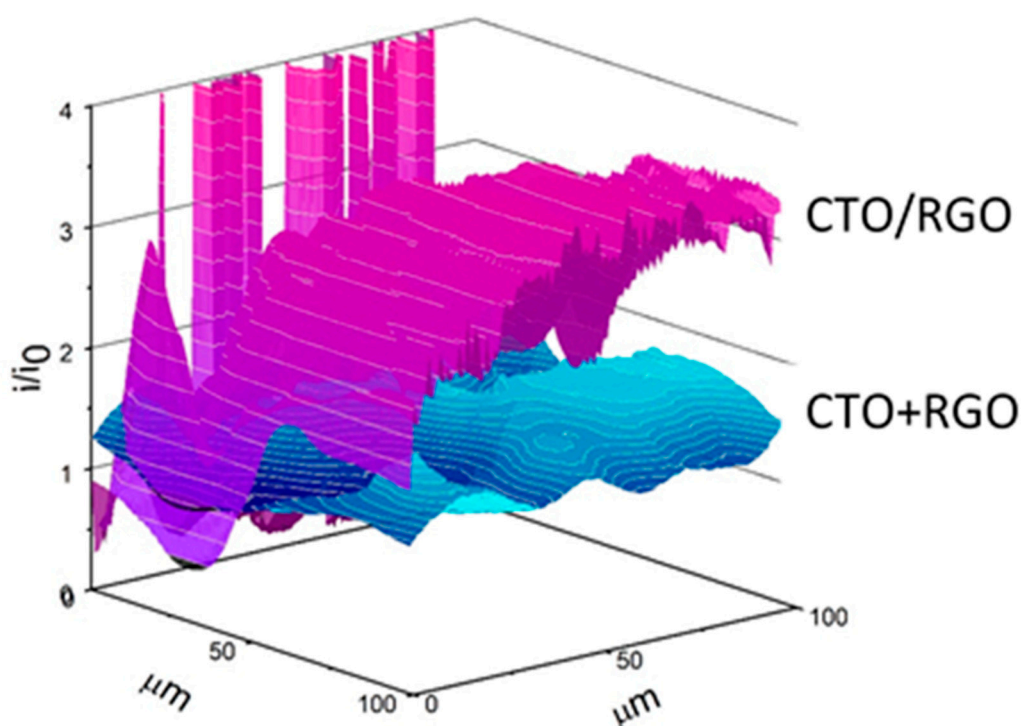


**Figure 6.** Scanning electrochemical microscopy (SECM) feedback plot for the CTO/RGO and CTO+RGO electrodes using ferrocene methanol as the redox mediator.

### 3.2. Electrochemical Behaviour of Glassy Carbon Electrodes Modified with the Hybrid Materials towards Hydrogen Peroxide

The electrocatalytic activity of the hybrid materials towards hydrogen peroxide was studied using a GCE modified with nanohybrids dispersed in Nafion<sup>®</sup>. Figure 7a shows the polarization curves for the reduction of hydrogen peroxide with GCEs modified with CTO+RGO and CTO/RGO. The onset potentials for the reduction of hydrogen peroxide at CTO/RGO and CTO+RGO were  $-0.180$  V and  $-0.210$  V, respectively, which were values lower than those reported for other similar hybrid materials of graphene and metallic oxides [75]. The current density obtained using CTO/RGO ( $0.952$  mA/cm<sup>2</sup>) was three times higher than that obtained using CTO+RGO ( $0.335$  mA/cm<sup>2</sup>). Thus, CTO/RGO exhibited better electrocatalytic activity towards hydrogen peroxide reduction. The selected

working potential for further studies was  $-0.400$  V, as this gave a sensitive and stable signal for the reduction of hydrogen peroxide.

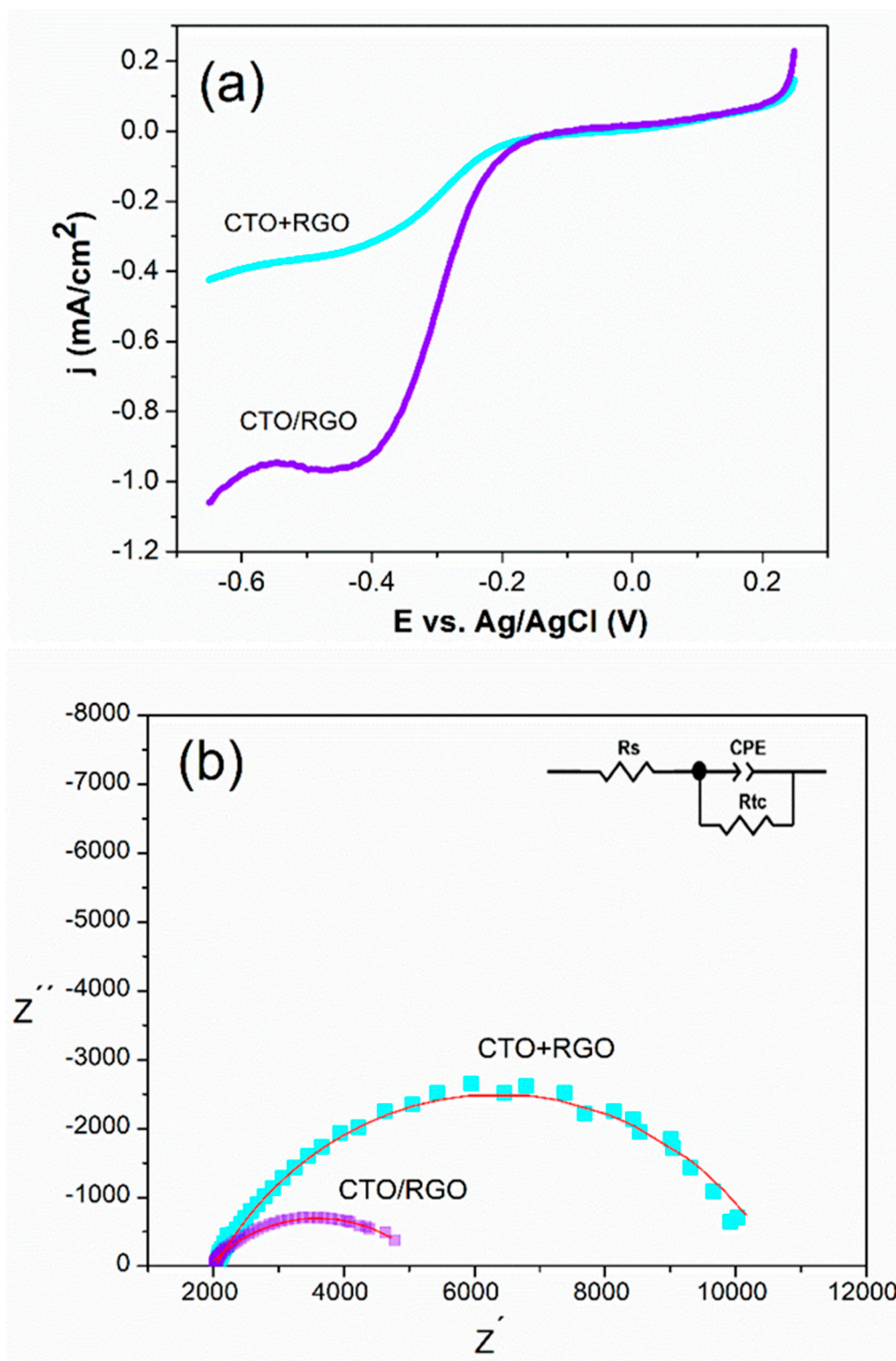


**Figure 7.** Polarization curves for reduction of 1.0 mM  $H_2O_2$  on GCEs modified with CTO/RGO and CTO+RGO hybrids in  $N_2$ -saturated pH 12 NaOH. Sweep rate of 5 mV/s and rotating speed of 1600 rpm (a). Nyquist plot of 1.0 mM  $H_2O_2$  on CTO/RGO and CTO+RGO hybrids in pH 12 NaOH at  $-0.400$  V. Inset on figure: Equivalent circuit. (b) The symbols represent the experimental results, and the solid line represents the corresponding fit with the equivalent circuit.

To obtain additional information about the behaviour of the nanohybrid-modified electrodes, we performed electrochemical impedance spectroscopy experiments at  $-0.400$  V, using hydrogen peroxide as the redox probe. Figure 7b shows the Nyquist plots obtained for the modified CTO/RGO and CTO+RGO glassy carbon electrodes. The equivalent circuit is  $(R_s(R_{ct}CPE))$  (displayed in the inset of Figure 7b), where  $R_s$  is the resistance of the solution,  $R_{ct}$  is the charge transfer resistance, and CPE is a constant phase element. The impedance is defined by Equation (1):

$$Z_{CPE} = \frac{1}{(j\omega)^n C} \quad (1)$$

where  $C$  is the capacitance and  $n$  is the parameter that indicates the behaviour of the CPE, varying between  $1 \geq n \geq 0$  [76]. Table 2 summarizes the different EIS parameters. It was determined that the electroactive area values for the CTO/RGO and CTO+RGO hybrids were similar ( $0.044 \pm 0.003$  cm<sup>2</sup> and  $0.045 \pm 0.004$ , respectively), however, there were differences in the capacitance values, indicating that there was no relationship with the number of active sites [77,78].

**Table 2.** EIS parameters obtained from the Nyquist plots shown in Figure 7.

Hybrid Material	C ( $10^{-5}$ F)	n	$R_{ct}$ ( $\Omega$ )
CTO+RGO	$1.6 \pm 0.1$	$0.68 \pm 0.02$	$8422 \pm 1591$
CTO/RGO	$8.4 \pm 1.9$	$0.51 \pm 0.01$	$3679 \pm 287$

A higher capacitance value for the CTO/RGO hybrid was related to an increased coupling between both nanomaterials; this increased interaction facilitated the transfer of charge and improved the electrochemical activity, which is reflected in the lower resistance ( $R_{ct}$ ).

### 3.3. Amperometric Detection of Hydrogen Peroxide

Figure 8a depicts the calibration plots obtained for CTO/RGO and CTO+RGO from amperometric experiments at  $-0.400$  V with additions of  $1.0 \times 10^{-4}$  M hydrogen peroxide, as shown in the inset. A clear and well-defined response was obtained with both electrodes, with a more sensitive response from the CTO/RGO electrode ( $110 \pm 3$   $\mu$ A/mMcm<sup>2</sup>) than that for the CTO+RGO electrode ( $54 \pm 4$   $\mu$ A/mMcm<sup>2</sup>). The detection limits (taken as  $3.3 \sigma/S$ , where  $\sigma$  is the standard deviation of the blank signal and  $S$  is the sensitivity) were  $2.1 \times 10^{-6}$  M and  $1.1 \times 10^{-6}$  M for CTO/RGO and CTO+RGO, respectively. The reproducibility values obtained for the different electrodes were 2.9% for CTO/RGO and 6.1% for CTO+RGO.

The strong coupling between CTO and RGO in the CTO/RGO hybrid can improve the dispersion of CTO nanoparticles on the surfaces of RGO during the synthetic procedure, decreasing the resistance and increasing the electrical conductivity of the final material. Also, the higher mesoporosity of the CTO/RGO hybrid allows the easy access of H<sub>2</sub>O<sub>2</sub> to active sites, as well as the accessibility of the electrolyte.

A comparative bar plot for the sensitivities obtained using GCEs modified with both materials separately (i.e., RGO, CTO, and with the hybrids CTO+RGO and CTO/RGO) is shown in Figure 8b. The results show that there is a clear synergistic effect when CTO and RGO are present as nanohybrid materials, either in the case of CTO/RGO or CTO+RGO, although the GCE modified with the nanohybrid material prepared in situ produces the highest sensitivity as a result of the intimate contact between the individual components. As the RGO was evaluated itself as an electrocatalyst, it is possible to conclude that the impurities reported for this material (see Supplementary Materials) do not influence the synergistic effect of the hybrid materials.

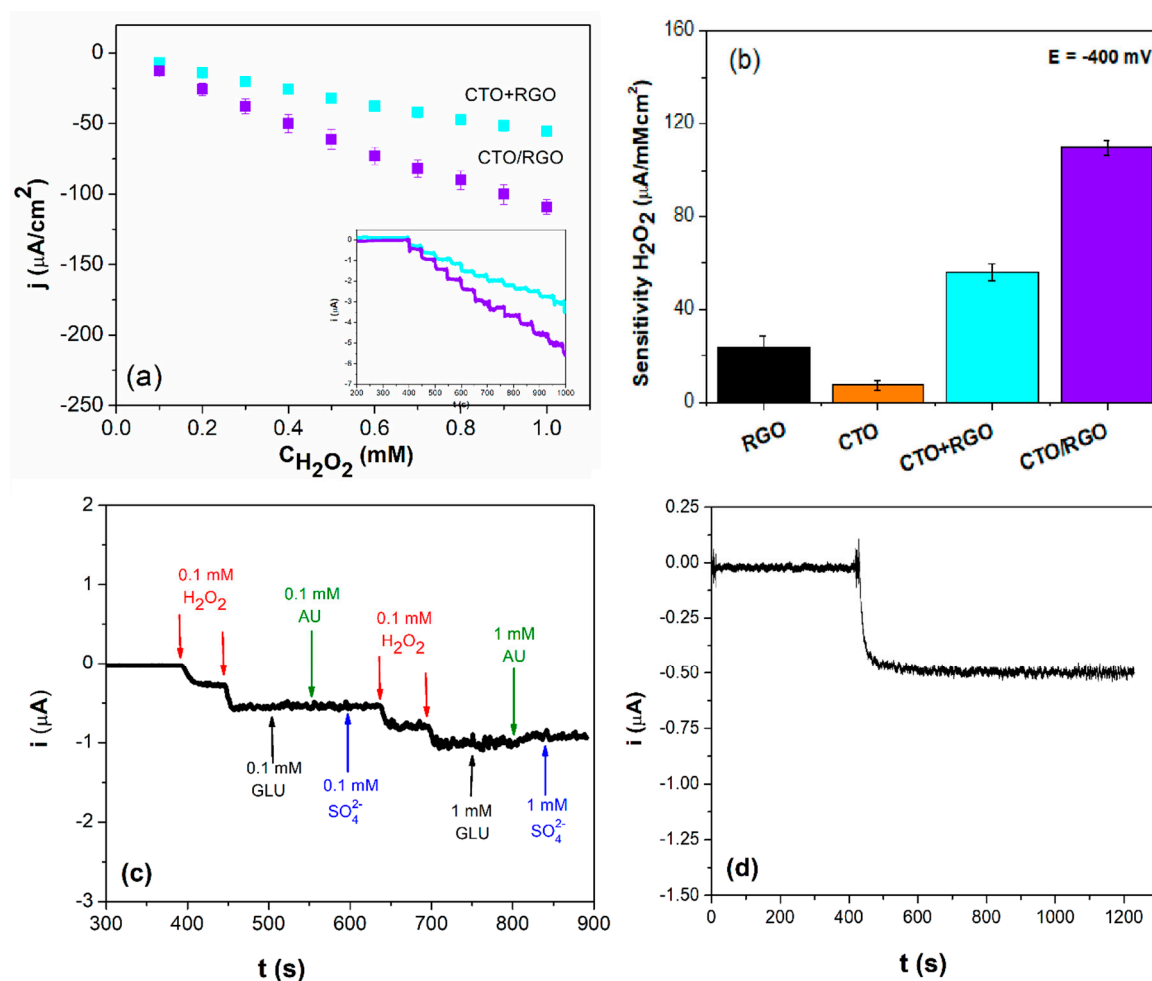


**Figure 8.** Current density vs.  $\text{H}_2\text{O}_2$  concentration plot, obtained from the amperometric experiment (a). Amperograms of CTO/RGO and CTO+RGO obtained after ten 0.1 mM  $\text{H}_2\text{O}_2$  additions (insert figure (a)). Sensitivity calculated for CTO/RGO, CTO+RGO, RGO, and CTO (b). Amperometric responses of the CTO/RGO to successive additions of  $\text{H}_2\text{O}_2$ , uric acid (AU), glucose (GLU), and sodium sulfate (c). Stability of the response to 1.0 mM  $\text{H}_2\text{O}_2$  for CTO/RGO (d) at  $-0.400$  V in pH 12 NaOH.

A comparison of our results with other reported analytical sensors based on RGO/metallic oxide composites or cobalt oxide alone is present in Table 3. As can be seen, our method presents Limit of Detection (LOD) comparable to those obtained with other methods, with a high sensitivity achieved using the lower applied potential (i.e., is more efficient than the other reported methods).

**Table 3.** Comparison of the analytical performance of various electrodes for  $\text{H}_2\text{O}_2$  sensing.

Electrode	Electrolyte	Potential (V)	Sensitivity ( $\mu\text{A}/\text{mM}^{-1}\text{cm}^{-2}$ )	LOD ( $\mu\text{M}$ )	Ref.
$\text{MnO}_2\text{-Co}_3\text{O}_4/\text{RGO}$	PBS (pH = 7.4)	+0.50	53.6	0.8	[79]
$\text{Co}_3\text{O}_4$	$\text{NaH}_2\text{PO}_4\text{-NaOH}$ (pH 10)	-0.70	-	4.4	[80]
$\text{Pt}/\text{Fe}_3\text{O}_4/\text{RGO}$	PBS (pH = 7.4)	0.00	6.56	1.56	[81]
$\text{NiCo}_2\text{S}_4/\text{RGO}$	NaOH (pH13)	-0.45	118.5	0.19	[82]
$\text{MnO}_2/\text{RGO}$	PBS (pH = 7.4)	-0.50	59.0	10	[83]
CTO/RGO-25	NaOH (pH12)	-0.40	106	2.1	(*)

(\*) This work.

Given that CTO/RGO showed better sensitivity, reproducibility, and a greater synergistic effect than that of the CTO+RGO, the selectivity and stability was evaluated with CTO/RGO-modified GCE.

Figure 8c displays the amperometric response of hydrogen peroxide for CTO/RGO at  $-0.400$  V after two additions of  $1.0 \times 10^{-4}$  M hydrogen peroxide and successive additions of glucose, uric acid (representing biological interferences), and sulfate (cleaning product interference). The CTO/RGO platform generated a negligible response in the presence of interferences, indicating a high selectivity for  $H_2O_2$  detection. Figure 8d shows the short-term stability of the amperometric response to  $1.0 \times 10^{-4}$  M hydrogen peroxide recorded over a continuous time period of 800 s. The response of the CTO/RGO electrode remained stable throughout the entire experiment, with only a 4.6% decrease in current. Finally, the response time of the surface after the addition of hydrogen peroxide was fast, taking no more than 10 s to establish a stable current.

Furthermore, to verify the applicability of the CTO/RGO hybrid material,  $H_2O_2$  detection was performed using a real sample (a commercial laundry whitening product, Vanish®). The results showed that our amperometric method detected a  $H_2O_2$  concentration value of  $(1.900 \pm 0.004)$  M, and the reference method (titration method) detected a concentration of  $(1.520 \pm 0.060)$  M. Both values were above the value declared by the manufacturer (1.25 M) but demonstrated future analytical usefulness for determining hydrogen peroxide content in real samples after an adequate treatment of the samples or the incorporation of an anti-interference membrane on the resulting electrodes.

#### 4. Conclusions

For the first time, the synthesis of nanostructured CTO at low temperature, alone and in the presence of RGO, and using a one-step hydrothermal synthesis method with new precursors and low temperatures is reported. The CTO/RGO and CTO+RGO hybrids demonstrated electrocatalytic activity towards the electroreduction of hydrogen peroxide. More importantly, a better coupling between CTO and RGO during the in situ synthesis process promoted an effective GCE/CTO/RGO electrode, which was shown to be an interesting and simple alternative for the quantification of hydrogen peroxide and which opens doors for further electrochemical sensor development.

**Supplementary Materials:** The following are available online at <http://www.mdpi.com/2079-4991/9/11/1611/s1>, Figure S1: Raman frequency shift for RGO in CTO/RGO hybrid, Figure S2: TGA curve of CTO/RGO, Figure S3: Histogram particle size distribution of CTO. Table S1: Elemental Analysis of RGO, supported by Graphenea, Table S2: X-ray fluorescence spectrometry analysis of RGO, supported by Graphenea, Table S3: Rietveld Refinement results summary.

**Author Contributions:** The manuscript was written with contributions from all authors. All authors have approved the final version of the manuscript.

**Funding:** Funding was provided by Conicyt-Fondecyt Chile (Grant N°1161225), Conicyt-FONDEQUIP Chile (Grant N° EQM170111), and Redes de Investigación 021842SG\_RED: RCNM-USACH “Red de Caracterización de NanoMateriales—Universidad de Santiago de Chile”. Additional funding was provided by Ministerio de Economía (MINECO, Spain) under project RTI2018-095303-B-C51.

**Acknowledgments:** The authors acknowledge financial support from Conicyt-Fondecyt CHILE (Grant N°1161225), Conicyt-FONDEQUIP Chile (Grant N° EQM170111), and Redes de Investigación 021842SG\_RED: RCNM-USACH “Red de Caracterización de NanoMateriales -USACH”, as well as MINECO (Spain) under project RTI2018-095303-B-C51. C.J. Venegas acknowledges the CONICYT scholarship for Ph.D. studies in Chile.

**Conflicts of Interest:** The authors declare no conflict of interest.

#### Abbreviations

CTO,  $Co_2TiO_4$ ; RGO, reduced oxide graphene; NPs, nanoparticles; CBNM, carbon-based nanomaterials.

#### References

1. Li, J.; Hu, H.; Li, H.; Yao, C. Recent developments in electrochemical sensors based on nanomaterials for determining glucose and its byproduct  $H_2O_2$ . *J. Mater. Sci.* **2017**, *52*, 10455–10469. [CrossRef]
2. Kumar, V.; Kumar, P.; Pournara, A.; Vellingiri, K.; Kim, K.H. Nanomaterials for the sensing of narcotics: Challenges and opportunities. *TrAC Trends Anal. Chem.* **2018**, *106*, 84–115. [CrossRef]

3. Karak, N. Fundamentals of Nanomaterials and Polymer Nanocomposites. In *Nanomaterials Polymer Nanocomposites*; Elsevier: Amsterdam, The Netherlands, 2019; pp. 1–45. [[CrossRef](#)]
4. Xu, J.; Wang, L. *Carbon Nanomaterials*; Elsevier Inc.: Amsterdam, The Netherlands, 2019. [[CrossRef](#)]
5. Wang, J. Nanomaterial-based electrochemical biosensors. *Analyst* **2005**, *130*, 421. [[CrossRef](#)] [[PubMed](#)]
6. Pumera, M.; Sánchez, S.; Ichinose, I.; Tang, J. Electrochemical nanobiosensors. *Sens. Actuators B Chem.* **2007**, *123*, 1195–1205. [[CrossRef](#)]
7. Pumera, M. Graphene-based nanomaterials and their electrochemistry. *Chem. Soc. Rev.* **2010**, *39*, 4146–4157. [[CrossRef](#)] [[PubMed](#)]
8. Baig, N.; Sajid, M.; Saleh, T.A. Recent trends in nanomaterial-modified electrodes for electroanalytical applications. *TrAC Trends Anal. Chem.* **2018**. [[CrossRef](#)]
9. Bo, X.; Zhou, M.; Guo, L. Electrochemical sensors and biosensors based on less aggregated graphene. *Biosens. Bioelectron.* **2017**, *89*. [[CrossRef](#)]
10. Novoselov, K.S.; Geim, A.K.; Morozov, S.; Jiang, D.; Katsnelson, M.I.; Grigorieva, I.V.; Dubonos, S.; Firsov, A.A. Two-dimensional gas of massless Dirac fermions in graphene. *Nature* **2005**, *438*, 197–200. [[CrossRef](#)]
11. Lee, C.; Wei, X.; Kysar, J.W.; Hone, J. Measurement of the Elastic Properties and Intrinsic Strength of Monolayer Graphene. *Science* **2008**, *321*, 385–388. [[CrossRef](#)]
12. Park, C.S.; Yoon, H.; Kwon, O.S. Graphene-based nanoelectronic biosensors. *J. Ind. Eng. Chem.* **2016**, *38*, 13–22. [[CrossRef](#)]
13. Bollella, P.; Fusco, G.; Tortolini, C.; Sanz, G.; Favero, G.; Gorton, L.; Antiochia, R. Beyond graphene: Electrochemical sensors and biosensors for biomarkers detection. *Biosens. Bioelectron.* **2017**, *89*, 152–166. [[CrossRef](#)] [[PubMed](#)]
14. Yang, W.; Ratinac, K.R.; Ringer, S.P.; Thordarson, P.; Gooding, J.J.; Braet, F. Carbon nanomaterials in biosensors: Should you use nanotubes or graphene? *Angew. Chem. Int. Ed.* **2010**, *49*, 2114–2138. [[CrossRef](#)] [[PubMed](#)]
15. Luo, X.; Morrin, A.; Killard, A.J.; Smyth, M.R. Application of nanoparticles in electrochemical sensors and biosensors. *Electroanalysis* **2006**, *18*, 319–326. [[CrossRef](#)]
16. Guo, S.; Du, Y.; Yang, X.; Dong, S.; Wang, E. Solid-State Label-Free Integrated Aptasensor Based on Graphene-Mesoporous Silica–Gold Nanoparticle Hybrids and Silver Microspheres. *Anal. Chem.* **2011**, *83*, 8035–8040. [[CrossRef](#)]
17. Gao, X.; Zhang, Y.; Wu, Q.; Chen, H.; Chen, Z.; Lin, X. One step electrochemically deposited nanocomposite film of chitosan-carbon nanotubes-gold nanoparticles for carcinoembryonic antigen immunosensor application. *Talanta* **2011**, *85*, 1980–1985. [[CrossRef](#)]
18. Chen, X.; Dong, Y.; Zhang, H.; Chen, X.; Hu, J.; Rahman, Z.U.; Su, L. Graphene oxide–Fe<sub>3</sub>O<sub>4</sub> magnetic nanocomposites with peroxidase-like activity for colorimetric detection of glucose. *Nanoscale* **2012**, *4*, 3969. [[CrossRef](#)]
19. Pradhan, G.K.; Padhi, D.K.; Parida, K.M. Fabrication of #-Fe<sub>2</sub>O<sub>3</sub> Nanorod/RGO composite: A novel hybrid photocatalyst for phenol degradation. *ACS Appl. Mater. Interfaces* **2013**, *5*, 9101–9110. [[CrossRef](#)]
20. Gong, C.; Bai, Y.J.; Feng, J.; Tang, R.; Qi, Y.X.; Lun, N.; Fan, R.H. Enhanced electrochemical performance of FeWO<sub>4</sub> by coating nitrogen-doped carbon. *ACS Appl. Mater. Interfaces* **2013**, *5*, 4209–4215. [[CrossRef](#)]
21. Galindo, R.; Gutiérrez, S.; Menéndez, N.; Herrasti, P. Catalytic properties of nickel ferrites for oxidation of glucose,  $\beta$ -nicotiamide adenine dinucleotide (NADH) and methanol. *J. Alloy Compd.* **2014**, *586*, 511–515. [[CrossRef](#)]
22. Liu, Z.; Wang, J.; Xie, D.; Chen, G. Polyaniline-Coated Fe<sub>3</sub>O<sub>4</sub> Nanoparticle-Carbon-Nanotube Composite and its Application in Electrochemical Biosensing. *Small* **2008**, *4*, 462–466. [[CrossRef](#)]
23. Mohamed, S.G.; Tsai, Y.Q.; Chen, C.J.; Tsai, Y.T.; Hung, T.F.; Chang, W.S.; Liu, R.S. Ternary Spinel MCo<sub>2</sub>O<sub>4</sub> (M = Mn, Fe, Ni, and Zn) Porous Nanorods as Bifunctional Cathode Materials for Lithium–O<sub>2</sub> Batteries. *ACS Appl. Mater. Interfaces* **2015**, *7*, 12038–12046. [[CrossRef](#)] [[PubMed](#)]
24. Kannan, P.K.; Late, D.J.; Morgan, H.; Rout, C.S. Recent developments in 2D layered inorganic nanomaterials for sensing. *Nanoscale* **2015**, *7*, 13293–13312. [[CrossRef](#)] [[PubMed](#)]
25. Bai, S.; Shen, X. Graphene–inorganic nanocomposites. *RSC Adv.* **2012**, *2*, 64–98. [[CrossRef](#)]
26. Huang, X.; Qi, X.; Boey, F.; Zhang, H. Graphene-based composites. *Chem. Soc. Rev.* **2012**, *41*, 666–686. [[CrossRef](#)]
27. Douafer, S.; Lahmar, H.; Benamira, M.; Rekhila, G.; Trari, M. Physical and photoelectrochemical properties of the spinel LiMn<sub>2</sub>O<sub>4</sub> and its application in photocatalysis. *J. Phys. Chem. Solids* **2018**, *118*, 62–67. [[CrossRef](#)]

28. Han, M.; Wang, Z.; Xu, Y.; Wu, R.; Jiao, S.; Chen, Y.; Feng, S. Physical properties of  $\text{MgAl}_2\text{O}_4$ ,  $\text{CoAl}_2\text{O}_4$ ,  $\text{NiAl}_2\text{O}_4$ ,  $\text{CuAl}_2\text{O}_4$ , and  $\text{ZnAl}_2\text{O}_4$  spinels synthesized by a solution combustion method. *Mater. Chem. Phys.* **2018**, *215*, 251–258. [[CrossRef](#)]
29. Kumar, R.T.; Suresh, P.; Selvam, N.C.S.; Kennedy, L.J.; Vijaya, J.J. Comparative study of nano copper aluminate spinel prepared by sol-gel and modified sol-gel techniques: Structural, electrical, optical and catalytic studies. *J. Alloy Compd.* **2012**, *522*, 39–45. [[CrossRef](#)]
30. Cherifi, K.; Rekhila, G.; Omeiri, S.; Bessekhoud, Y.; Trari, M. Physical and photoelectrochemical properties of the spinel  $\text{ZnCr}_2\text{O}_4$  prepared by sol gel: Application to Orange II degradation under solar light. *J. Photochem. Photobiol. A Chem.* **2019**, *368*, 290–295. [[CrossRef](#)]
31. Jin, S.; Yang, G.; Song, H.; Cui, H.; Wang, C. Ultrathin Hexagonal 2D  $\text{Co}_2\text{GeO}_4$  Nanosheets: Excellent Li-Storage Performance and ex situ Investigation of Electrochemical Mechanism. *ACS Appl. Mater. Interfaces* **2015**, *7*, 24932–24943. [[CrossRef](#)]
32. Wang, Y.; Zhao, X.S.; Lv, M.; Wang, B.; Cui, L.; Guo, P. Facile Synthesis of  $\text{ZnFe}_2\text{O}_4$  Nanoparticles with Tunable Magnetic and Sensing Properties. *Langmuir* **2013**, *29*, 8997–9003. [[CrossRef](#)]
33. Mahathesha, K.R.; Chandra, U.; Reddy, S.; Kumara Swamy, B.E.; Jayadevappa, H.; Sathisha, T.V. Synthesis of  $\text{MgFe}_2\text{O}_4$  nanoparticles and  $\text{MgFe}_2\text{O}_4$  nanoparticles/CPE for electrochemical investigation of dopamine. *Anal. Methods* **2011**, *3*, 2792. [[CrossRef](#)]
34. Qi, X.; Gao, H.; Zhang, Y.; Wang, X.; Chen, Y.; Sun, W. Electrochemical DNA biosensor with chitosan- $\text{Co}_3\text{O}_4$  nanorod-graphene composite for the sensitive detection of staphylococcus aureus nuc gene sequence. *Bioelectrochemistry* **2012**, *88*, 42–47. [[CrossRef](#)] [[PubMed](#)]
35. Wang, H.W.; Hu, Z.A.; Chang, Y.Q.; Chen, Y.L.; Zhang, Z.Y.; Yang, Y.Y.; Wu, H.Y. Preparation of reduced graphene oxide/cobalt oxide composites and their enhanced capacitive behaviors by homogeneous incorporation of reduced graphene oxide sheets in cobalt oxide matrix. *Mater. Chem. Phys.* **2011**, *130*, 672–679. [[CrossRef](#)]
36. Venegas, C.J.; Yedinak, E.; Marco, J.F.; Bollo, S. Ruiz-León, D. Co-doped stannates /reduced graphene composites: Effect of cobalt substitution on the electrochemical sensing of hydrogen peroxide. *Sens. Actuators B Chem.* **2017**, *250*. [[CrossRef](#)]
37. Yang, X.; Ouyang, Y.; Wu, F.; Hu, Y.; Zhang, H.; Wu, Z. In situ & controlled preparation of platinum nanoparticles doping into graphene sheets@cerium oxide nanocomposites sensitized screen printed electrode for nonenzymatic electrochemical sensing of hydrogen peroxide. *J. Electroanal. Chem.* **2016**, *777*, 85–91. [[CrossRef](#)]
38. Deepalakshmi, T.; Tran, D.T.; Kim, N.H.; Chong, K.T.; Lee, J.H. Nitrogen-Doped Graphene-Encapsulated Nickel Cobalt Nitride as a Highly Sensitive and Selective Electrode for Glucose and Hydrogen Peroxide Sensing Applications. *ACS Appl. Mater. Interfaces* **2018**, *10*, 35847–35858. [[CrossRef](#)]
39. Zhang, C.; Li, L.; Ju, J.; Chen, W. Electrochemical sensor based on graphene-supported tin oxide nanoclusters for nonenzymatic detection of hydrogen peroxide. *Electrochim. Acta* **2016**, *210*, 181–189. [[CrossRef](#)]
40. Newman, J.D.; Turner, A.P.F. Home blood glucose biosensors: A commercial perspective. *Biosens. Bioelectron.* **2005**, *20*, 2435–2453. [[CrossRef](#)]
41. Chen, W.; Cai, S.; Ren, Q.Q.; Wen, W.; Di Zhao, Y. Recent advances in electrochemical sensing for hydrogen peroxide: A review. *Analyst* **2012**, *137*, 49–58. [[CrossRef](#)]
42. Maksoud, M.I.A.A.; El-Sayyad, G.S.; Ashour, A.H.; El-Batal, A.I.; Elsayed, M.A.; Gobara, M.; El-Khawaga, A.M.; Abdel-Khalek, E.K.; El-Okr, M.M. Antibacterial, antibiofilm, and photocatalytic activities of metals-substituted spinel cobalt ferrite nanoparticles. *Microb. Pathog.* **2019**, *127*, 144–158. [[CrossRef](#)]
43. Šutka, A.; Gross, K.A. Spinel ferrite oxide semiconductor gas sensors. *Sens. Actuators B Chem.* **2016**, *222*, 95–105. [[CrossRef](#)]
44. Kharisov, B.I.; Dias, H.V.R.; Kharissova, O.V. Mini-review: Ferrite nanoparticles in the catalysis. *Arab. J. Chem.* **2014**. [[CrossRef](#)]
45. Peng, D.; Liu, X.; Huang, M.; Liu, R. Characterization of a Novel  $\text{Co}_2\text{TiO}_4$  Nanopowder for the Rapid Identification of Latent and Blood Fingerprints. *Anal. Lett.* **2018**, *51*, 1796–1808. [[CrossRef](#)]
46. Ramezani, M.; Hosseinpour-Mashkani, S.M. Controlled Synthesis, Characterization, and Photocatalytic Application of  $\text{Co}_2\text{TiO}_4$  Nanoparticles. *J. Electron. Mater.* **2016**, *2–8*. [[CrossRef](#)]
47. Yankin, A.; Vikhrev, O.; Balakirev, V. P–T–x diagram of the Co–Ti–O system. *J. Phys. Chem. Solids* **1999**, *60*, 139–143. [[CrossRef](#)]



48. Nayak, S.; Thota, S.; Joshi, D.C.; Krautz, M.; Waske, A.; Behler, A.; Eckert, J.; Sarkar, T.; Andersson, M.S.; Mathieu, R.; et al. Magnetic compensation, field-dependent magnetization reversal, and complex magnetic ordering in  $\text{Co}_2\text{TiO}_4$ . *Phys. Rev. B* **2015**, *92*, 214434. [[CrossRef](#)]
49. Sakamoto, N. Magnetic Properties of Cobalt Titanate. *J. Phys. Soc. Jpn.* **1962**, *17*, 99–102. [[CrossRef](#)]
50. Habibi, M.H.; Shojaei, E. Synthesis of cobalt-orthotitanate inverse spinel nano particles via a novel low temperature solvothermal method: Structural, opto-electronical, morphological, surface characterization and photo-catalytical application in mineralization of Remazol Red RB 1. *J. Mater. Sci. Mater. Electron.* **2017**. [[CrossRef](#)]
51. Yuvaraj, S.; Vignesh, R.H.; Vasylechko, L.; Lee, Y.S.; Selvan, R.K. Synthesis and electrochemical performance of  $\text{Co}_2\text{TiO}_4$  and its core-shell structure of  $\text{Co}_2\text{TiO}_4@\text{C}$  as negative electrodes for Li-ion batteries. *RSC Adv.* **2016**, *6*, 69016–69026. [[CrossRef](#)]
52. Toby, B.H. EXPGUI, a graphical user interface for GSAS. *J. Appl. Crystallogr.* **2001**, *34*, 210–213. [[CrossRef](#)]
53. Larson, A.C.; Von Dreele, R.B. General Structural Analysis System (GSAS), Los Alamos National Laboratory Report LAUR 86-748 (2000).
54. Mohai, M. XPS MultiQuant: Multimodel XPS quantification software. *Surf. Interface Anal.* **2004**, *36*, 828–832. [[CrossRef](#)]
55. Brunauer, S.; Emmett, P.H.; Teller, E. Adsorption of Gases in Multimolecular Layers. *J. Am. Chem. Soc.* **1938**, *60*, 309–319. [[CrossRef](#)]
56. Yang, S.; Feng, X.; Ivanovici, S.; Müllen, K. Fabrication of Graphene-Encapsulated Oxide Nanoparticles: Towards High-Performance Anode Materials for Lithium Storage. *Angew. Chem. Int. Ed.* **2010**, *49*, 8408–8411. [[CrossRef](#)] [[PubMed](#)]
57. Ding, S.; Luan, D.; Boey, F.Y.C.; Chen, J.S.; Lou, X.W.D.  $\text{SnO}_2$  nanosheets grown on graphene sheets with enhanced lithium storage properties. *Chem. Commun.* **2011**, *47*, 7155–7157. [[CrossRef](#)]
58. Mahmoudian, M.R.; Alias, Y.; Basirun, W.J.; Woi, P.M.; Sookhajian, M. Facile preparation of  $\text{MnO}_2$  nanotubes/reduced graphene oxide nanocomposite for electrochemical sensing of hydrogen peroxide. *Sens. Actuators B Chem.* **2014**, *201*, 526–534. [[CrossRef](#)]
59. Liang, Y.; Wang, H.; Zhou, J.; Li, Y.; Wang, J.; Regier, T.; Dai, H. Covalent hybrid of spinel manganese-cobalt oxide and graphene as advanced oxygen reduction electrocatalysts. *J. Am. Chem. Soc.* **2012**, *134*, 3517–3523. [[CrossRef](#)]
60. Thota, S.; Reehuis, M.; Maljuk, A.; Hoser, A.; Hoffmann, J.U.; Weise, B.; Waske, A.; Krautz, M.; Joshi, D.C.; Nayak, S.; et al. Neutron diffraction study of the inverse spinels  $\text{Co}_2\text{TiO}_4$  and  $\text{Co}_2\text{SnO}_4$ . *Phys. Rev. B* **2017**, *96*, 144104. [[CrossRef](#)]
61. Báez, D.; Pardo, H.; Laborda, I.; Marco, J.F.; Yáñez, C.; Bollo, S. Reduced Graphene Oxides: Influence of the Reduction Method on the Electrocatalytic Effect towards Nucleic Acid Oxidation. *Nanomaterials* **2017**, *7*, 168. [[CrossRef](#)]
62. Konios, D.; Stylianakis, M.M.; Stratakis, E.; Kymakis, E. Dispersion behaviour of graphene oxide and reduced graphene oxide. *J. Colloid Interface Sci.* **2014**, *430*, 108–112. [[CrossRef](#)]
63. Marco, J.F.; Gancedo, J.R.; Ortiz, J.; Gautier, J.L. Characterization of the spinel-related oxides  $\text{Ni}_x\text{Co}_{3-x}\text{O}_4$  ( $x = 0.3, 1.3, 1.8$ ) prepared by spray pyrolysis at 350 °C. *Appl. Surf. Sci.* **2004**, *227*, 175–186. [[CrossRef](#)]
64. Nayak, S.; Dasari, K.; Joshi, D.C.; Pramanik, P.; Palai, R.; Sathe, V.; Chauhan, R.N.; Tiwari, N.; Thota, S. Spectroscopic studies of  $\text{Co}_2\text{TiO}_4$  and  $\text{Co}_3\text{O}_4$  two-phase composites. *Phys. Status Solidi* **2016**, *253*, 2270–2282. [[CrossRef](#)]
65. Walczak, M.; Papadopoulou, E.L.; Sanz, M.; Manousaki, A.; Marco, J.F.; Castillejo, M. Structural and morphological characterization of  $\text{TiO}_2$  nanostructured films grown by nanosecond pulsed laser deposition. *Appl. Surf. Sci.* **2009**, *255*, 5267–5270. [[CrossRef](#)]
66. Sanz, M.; Walczak, M.; de Nalda, R.; Oujja, M.; Marco, J.F.; Rodriguez, J.; Izquierdo, J.G.; Bañares, L.; Castillejo, M. Femtosecond pulsed laser deposition of nanostructured  $\text{TiO}_2$  films. *Appl. Surf. Sci.* **2009**, *255*, 5206–5210. [[CrossRef](#)]
67. Walczak, M.; Oujja, M.; Marco, J.F.; Sanz, M.; Castillejo, M. Pulsed laser deposition of  $\text{TiO}_2$ : Diagnostic of the plume and characterization of nanostructured deposits. *Appl. Phys. A* **2008**, *93*, 735–740. [[CrossRef](#)]
68. Marco, J.F.; Ramón Gancedo, J.R.; Berry, F.J. The oxidation states of titanium and niobium in compounds of composition  $\text{Sn}_x\text{NbTiP}_3\text{O}_{12}$  ( $0 < x \leq 0.50$ ): An XPS study. *Polyhedron* **1997**, *16*, 2957–2961. [[CrossRef](#)]

69. Atuchin, V.V.; Kesler, V.G.; Pervukhina, N.V.; Zhang, Z. Ti 2p and O 1s core levels and chemical bonding in titanium-bearing oxides. *J. Electron Spectrosc. Relat. Phenom.* **2006**, *152*, 18–24. [[CrossRef](#)]
70. Mazarío, E.; Herrasti, P.; Morales, M.P.; Menéndez, N. Synthesis and characterization of CoFe<sub>2</sub>O<sub>4</sub> ferrite nanoparticles obtained by an electrochemical method. *Nanotechnology* **2012**, *23*, 355708. [[CrossRef](#)]
71. Thommes, M.; Kaneko, K.; Neimark, A.V.; Olivier, J.P.; Rodriguez-Reinoso, F.; Rouquerol, J.; Sing, K.S.W. Physisorption of gases, with special reference to the evaluation of surface area and pore size distribution (IUPAC Technical Report). *Pure Appl. Chem.* **2015**, *87*, 1051–1069. [[CrossRef](#)]
72. Khanahmadzadeh, S.; Enhessari, M.; Solati, Z.; Mohebalizadeh, A.; Alipouramjad, A. Synthesis, characterization and optical band gap of the Co<sub>2</sub>TiO<sub>4</sub> nanoparticles. *Mater. Sci. Semicond. Process.* **2015**, *31*, 599–603. [[CrossRef](#)]
73. Primo, E.N.; Gutierrez, F.A.; Luque, G.L.; Dalmasso, P.R.; Gasnier, A.; Jalit, Y.; Moreno, M.; Bracamonte, M.V.; Rubio, M.E.; Pedano, M.L.; et al. Comparative study of the electrochemical behavior and analytical applications of (bio)sensing platforms based on the use of multi-walled. *Anal. Chim. Acta* **2013**, *805*, 19–35. [[CrossRef](#)]
74. González-Segura, K.; Cañete-Rosales, P.; delRio, R.; Yáñez, C.; Ferreyra, N.F.; Rivas, G.A.; Bollo, S. Effect of the Dispersing Agent on the Electrochemical Response of Glassy Carbon Electrodes Modified with Dispersions of Carbon Nanotubes. *Electroanalysis* **2012**, *24*, 2317–2323. [[CrossRef](#)]
75. Yedinak, E.; Venegas, C.J.; Brito, T.P.; Ruiz-León, D.; Bollo, S. Co<sub>2</sub>SnO<sub>4</sub>/Carbon Nanotubes Composites: A Novel Approach for Electrochemical Sensing of Hydrogen Peroxide. *Electroanalysis* **2017**, 1–5. [[CrossRef](#)]
76. Orazem, M.E.; Tribollet, B. Electrochemical Impedance Spectroscopy. *Annu. Rev. Anal. Chem.* **2010**, *3*, 207–229. [[CrossRef](#)]
77. Kerner, Z.; Pajkossy, T. On the origin of capacitance dispersion of rough electrodes. *Electrochim. Acta* **2000**, *46*, 207–211. [[CrossRef](#)]
78. Kerner, Z.; Pajkossy, T. Impedance of rough capacitive electrodes: The role of surface disorder. *J. Electroanal. Chem.* **1998**, *448*, 139–142. [[CrossRef](#)]
79. Li, S.J.; Xing, Y.; Yang, H.Y.; Huang, J.Y.; Wang, W.T.; Liu, R.T. Electrochemical synthesis of a binary Mn-Co oxides decorated graphene nanocomposites for application in nonenzymatic H<sub>2</sub>O<sub>2</sub> sensing. *Int. J. Electrochem. Sci.* **2017**, *12*, 6566–6576. [[CrossRef](#)]
80. Mu, J.; Zhang, L.; Zhao, M.; Wang, Y. Co<sub>3</sub>O<sub>4</sub> nanoparticles as an efficient catalase mimic: Properties, mechanism and its electrocatalytic sensing application for hydrogen peroxide. *J. Mol. Catal. A Chem.* **2013**, *378*, 30–37. [[CrossRef](#)]
81. Zhao, X.; Li, Z.; Chen, C.; Wu, Y.; Zhu, Z.; Zhao, H.; Lan, M. A Novel Biomimetic Hydrogen Peroxide Biosensor Based on Pt Flowers-decorated Fe<sub>3</sub>O<sub>4</sub>/Graphene Nanocomposite. *Electroanalysis* **2017**, *29*, 1518–1523. [[CrossRef](#)]
82. Wang, M.; Ma, J.; Guan, X.; Peng, W.; Fan, X.; Zhang, G.; Zhang, F.; Li, Y. A novel H<sub>2</sub>O<sub>2</sub> electrochemical sensor based on NiCo<sub>2</sub>S<sub>4</sub> functionalized reduced graphene oxide. *J. Alloy Compd.* **2019**, *784*, 827–833. [[CrossRef](#)]
83. Dong, S.; Xi, J.; Wu, Y.; Liu, H.; Fu, C.; Liu, H.; Xiao, F. High loading MnO<sub>2</sub> nanowires on graphene paper: Facile electrochemical synthesis and use as flexible electrode for tracking hydrogen peroxide secretion in live cells. *Anal. Chim. Acta* **2015**, *853*, 200–206. [[CrossRef](#)]

